

1 ~~PB: Large-Scale Clustering of Tropical Precipitation and its Implications for the Radiation~~  
2 ~~Budget across Timescales~~ Large-Scale Clustering of Tropical  
3 Precipitation in Interannual Variability and in a  
4 Warming Climate: Mechanisms and Implications for the  
5 Radiation Budget

6 **P. Blackberg<sup>1,2</sup>, M. S. Singh<sup>1,2</sup>**

7 <sup>1</sup>School of Earth, Atmosphere, and Environment, Monash University, Victoria, Australia  
8 <sup>2</sup>Centre of Excellence for the Weather of the 21st Century, Monash University, Victoria, Australia

---

Corresponding author: P. Blackberg, [carlphiliposcar@gmail.com](mailto:carlphiliposcar@gmail.com)

**9 Abstract**

10 The spatial organization of deep convection in tropical regions is posited to play an im-  
11 portant role in determining characteristics of the tropical climate such as the humidity  
12 distribution and cloudiness and may therefore be an important control on climate feed-  
13 backs. This study analyzes one aspect of convective organization, the clustering of heavy  
14 precipitation on large scales, in both interannual variability and under warming in fu-  
15 ture climate projections. Both observations and global climate models indicate that large-  
16 scale clustering is sensitive to the SST gradient in the Pacific, being largest during El  
17 Niño events. Under future warming, models project an increase in clustering with a large  
18 intermodel spread. The increase is associated with a narrowing of the intertropical con-  
19 vergence zone, while the model spread is partially explained by differences in projections  
20 of the SST gradient in the Pacific. Both observations and models indicate large-scale clus-  
21 tering influences the cloud and humidity distributions, albeit with some differences. How-  
22 ever, the intermodel spread in changes in clustering with warming is not related to the  
23 intermodel spread in projections of tropical-mean relative humidity or low cloudiness in  
24 regions of descent, precluding attempts to provide an observational constraint on feed-  
25 backs or climate sensitivity. Nevertheless, the tendency for a meridional contraction of  
26 precipitation explains about 45% of the variance in projected drying, highlighting the  
27 narrowing of the ITCZ as an important aspect of large-scale convective organization in  
28 a warmer climate.

**29 Plain Language Summary**

30 The spatial distribution of rainfall in the tropics is expected to change in a warm-  
31 ing climate, with potentially important impacts on how much radiation is absorbed by  
32 water vapor and reflected by clouds. This study shows that heavy rainfall tends to move  
33 towards the equator and to the Pacific Ocean in projections with global climate mod-  
34 els, resulting in an overall increase in the "clustering" of rainfall on the large scale. Fur-  
35 ther, the results show a shift in rainfall to the equator with global warming is associated  
36 with a drying of the tropical atmosphere, which may have an influence on how much the  
37 planet warms for a given  $CO_2$  change. However, similar observed shifts in rainfall in the  
38 current climate are not found to have the same effect on humidity and clouds as for changes  
39 with warming, suggesting caution should be exercised when using relationships derived  
40 from observations to predict future changes.

## 41 1 Introduction

42 The spatial organization of deep convection in tropical regions plays a critical role  
 43 in shaping the hydrological cycle and the moisture and cloud distribution (Hartmann  
 44 et al., 1984). Changes in organization with warming may therefore have implications for  
 45 a range of climatic processes, including precipitation extremes (e.g., Pendergrass et al.,  
 46 2016; Bao et al., 2017; Semie & Bony, 2020) and the radiative feedbacks that control equi-  
 47 librium climate sensitivity (ECS) (e.g., Emanuel et al., 2014; Bony et al., 2020; Schiro  
 48 et al., 2022). However, because many of the relevant small-scale processes are not resolved  
 49 in climate models, it remains unclear how convective organization will evolve in a warmer  
 50 climate.

51 While there are numerous ways by which convection may organize, one important  
 52 mechanism is the clumping or clustering together of convective elements (e.g., Maddox,  
 53 1980; Mapes, 1993; Bretherton et al., 2005). Such clustering occurs on a range of scales  
 54 (Mapes & Houze, 1993), including at large scales that are resolved by climate models  
 55 and at mesoscales that can typically only be resolved in high-resolution storm-resolving  
 56 simulations. Recently, Bläckberg & Singh (2022) showed that the extent to which trop-  
 57 ical precipitation exhibits clustering on the large scale increases with warming in climate  
 58 projections from the Coupled Model Intercomparison Project phase 5 (CMIP5). This  
 59 large-scale clustering is distinct from other types of organization on the mesoscale, but  
 60 idealized simulations suggest that similar processes may act at both scales, and that both  
 61 large-scale and mesoscale organization of convection may modulate the radiation bud-  
 62 get (Wing et al., 2018).

63 Here we build on the work of Bläckberg & Singh (2022), showing that increased  
 64 clustering of heavy precipitation with warming is a robust feature of the more recent CMIP6  
 65 as well as CMIP5. Further, we explore the mechanisms that lead to large-scale cluster-  
 66 ing of precipitation in the tropics and the influence of an increase in clustering on prop-  
 67 erties of the atmosphere that are important for the radiation budget. The analysis will  
 68 compare how clustering varies across different timescales, from interannual variability  
 69 in both models and observations to changes in the climatological clustering of convec-  
 70 tion in a warming climate. This approach allows us to assess whether observational con-  
 71 straints of convective organization under current climate conditions can help constrain  
 72 changes in organization and the associated radiative feedbacks with warming.

73 Previous studies have highlighted observed relationships between convective organi-  
 74 zation and the tropical radiation budget (Tobin et al., 2013; Holloway et al., 2017; Bony  
 75 et al., 2020). For example, Bony et al. (2020) find tropical mesoscale convective organi-  
 76 zation and Estimated Inversion Strength (EIS) in subsidence regions are the two strongest  
 77 predictors of deseasonalized monthly anomalies in net top-of-atmosphere radiation, to-  
 78 gether explaining about 60 percent of the variance. While the two predictors are signif-  
 79 icantly correlated and potentially partly mechanistically connected (Williams et al., 2023),  
 80 the authors find that both have an independent contribution in influencing the tropical  
 81 radiation budget; EIS is found to have a stronger correlation with the cloudy component  
 82 of the radiation budget while convective organization is found to have a stronger con-  
 83 nection to the clear-sky component of the radiation budget. Bony et al. (2020) argue that  
 84 clustering of deep convective elements is associated with a tropical-mean drying, result-  
 85 ing in increased outgoing longwave radiation due to a reduction in the greenhouse effect.  
 86 This hypothesis is supported by idealized studies of convective “self-aggregation” (e.g.,  
 87 Wing & Emanuel, 2014). Both cloud-resolving and climate-model simulations run in ide-  
 88 alized settings reminiscent of tropical conditions (i.e., low rotation rate and weak tem-  
 89 perature gradients) show increased outgoing longwave radiation when convection is more  
 90 clustered within the domain (Wing et al., 2018).

91 The preceding studies suggest that increased clustering of convection with warm-  
 92 ing may lead to a negative clear-sky feedback from clustering-induced drying, resulting

93 in reduced equilibrium climate sensitivity (ECS) (Emanuel et al., 2014). However, re-  
94 cent research suggests that clustering of deep convection on the large scale may also be  
95 indirectly connected to a positive shortwave feedback on warming through changes in  
96 low clouds (Schiro et al., 2022). According to this argument, drying associated with in-  
97 creased clustering of convection is controlled by the large-scale overturning circulation  
98 and is most pronounced in regions of climatological descent where low-cloudiness is sen-  
99 sitive to changes in relative humidity. The associated cloud changes then lead to a net  
100 positive feedback.

101 As the above discussion highlights, an important control on convective organiza-  
102 tion at both large- and mesoscales comes from large-scale circulation patterns, includ-  
103 ing the Intertropical Convergence Zone (ITCZ), the South Pacific Convergence Zone (SPCZ),  
104 the Walker circulation, and convectively-coupled tropical waves (Bony et al., 2020; Quan  
105 et al., 2025; Arnold & Randall, 2015; Wodzicki & Rapp, 2016; Wheeler & Kiladis, 1999).  
106 Changes to the clustering of precipitation under warming may therefore be linked to, for  
107 example, a “narrowing” of the ITCZ due to constraints on the export of energy by the  
108 Hadley cell (Byrne & Schneider, 2016) or changes in the Walker circulation driven by  
109 changes in zonal SST gradients (Quan et al., 2025), which may be associated with “El  
110 Nino-like” shifts in the SST climatology (Watanabe et al., 2024).

111 In this study we explore how the spatial distribution of heavy precipitation changes  
112 with increased large-scale clustering, demonstrating the importance of both meridional  
113 contractions and zonal shifts in convection. We further show that the effect of large-scale  
114 clustering on low clouds and moisture—key variables that control the radiation budget—  
115 varies with timescale and between global climate models and observations, making it dif-  
116 ficult to apply constraints from observed variability to a warmer climate. The paper is  
117 structured as follows. First we describe the datasets used and our quantification of large-  
118 scale clustering of precipitation (Section 2). Then we present the geographical spatial  
119 patterns of heavy precipitation that are associated with a high level of clustering (Sec-  
120 tion 3). After that, we connect the spatial patterns to leading mechanisms driving clus-  
121 tering (Section 4). Finally, we present the moisture and low-cloud distribution associ-  
122 ated with clustering (Section 5). Section 6 gives a summary of the key findings and an  
123 outlook for future research.

124 **2 Data and Methods**

125 Our analysis is focused on variations in the large-scale clustering of heavy precip-  
 126 itation in the tropics and its relationship to the atmospheric state in both observations  
 127 and an ensemble of global climate models (GCMs) primarily from CMIP6. We begin by  
 128 describing the datasets (both model and observational) used, before we describe the quan-  
 129 tification of large-scale clustering, and our analysis framework.

130 **2.1 Models**

131 We use simulations from 27 GCMs from CMIP6 (Eyring et al., 2016), using data  
 132 from the years 1970-1999 in the historical scenario, representing the current climate, and  
 133 from the years 2070-2099 under the Shared Socioeconomic Pathway 585 (SSP5-8.5), rep-  
 134 resenting a warmer climate. The models are chosen based on availability of the required  
 135 variables and are shown in Figure 5. We use one ensemble member from each model.

136 In addition to the CMIP6 models, we also consider a simulation using a high-resolution  
 137 GCM referred to here as IFS\_9\_FESOM\_5 (Koldunov et al., 2023). The Deutsches Kli-  
 138 marechenzentrum (DKRZ) Next Generation Earth Modelling Systems (NextGEMS) pre-  
 139 final cycle provides high-resolution globally simulated atmospheric and oceanic variables  
 140 for SSP3-7.0 forcing between 2025-2049 using the ECMWF Integrated Forecasting Sys-  
 141 tem (IFS) at  $\sim 9$  km horizontal grid spacing for the atmosphere and the Finite-VolumE  
 142 Sea Ice-Ocean model version 2 (FESOM2) at 5 km horizontal grid spacing for the ocean  
 143 (Koldunov et al., 2023). Although the model is at high resolution compared to the CMIP6  
 144 models, it retains a convection parameterization, and we therefore describe it as a GCM  
 145 rather than a storm-resolving model. Because the climate change signal during the sim-  
 146 ulation is small, we only use the high-resolution GCM to characterize interannual vari-  
 147 ability, using all available years.

148 **2.2 Observations**

149 Observed clustering of tropical precipitation is quantified based on daily precip-  
 150 itation estimates from the National Oceanic and Atmospheric Administration Global Pre-  
 151 cipitation Climatology Project (NOAA-GPCP) (Huffman et al., 2023), using the method  
 152 described in the next subsection. We further use NOAA-GlobalTemp (Huang et al., 2024),  
 153 and Clouds and the Earth's Radiant Energy System (CERES) data (NOAA Physical Sci-  
 154 ences Laboratory, Climate Prediction Center, 2025) to provide observational estimates  
 155 of surface temperature and outgoing longwave radiation, respectively. Estimates of ver-  
 156 tical pressure velocity and specific and relative humidity are taken from the fifth gen-  
 157 eration of the European Centre for Medium-Range Weather Forecasts reanalysis (ERA5)  
 158 (Hersbach et al., 2023). Apart from precipitation, all variables are taken as monthly av-  
 159 erages.

160 Finally, we develop a simple estimate of the low-cloud fraction using the tropical  
 161 weather states defined in Tselioudis et al. (2010) based on data from the International  
 162 Satellite Cloud Climatology Project (ISCCP) (Young et al., 2018). Tselioudis et al. (2010)  
 163 used a clustering algorithm to categorize histograms of cloud-top pressure and optical  
 164 thickness given by the ISCCP D1 dataset into a series of weather states defined in three  
 165 hourly polar-orbiting satellite scans with daily global coverage on a  $1^\circ \times 1^\circ$  grid. Each  
 166 weather state is characterized by a histogram in cloud-top pressure and optical thick-  
 167 ness that represents the centroid over all members of that weather state. Here we esti-  
 168 mate the cloud fraction as a function of pressure for a given weather state as the total  
 169 frequency of clouds of all optical thicknesses in a given range of cloud-top pressure within  
 170 the corresponding centroid histogram. We then calculate the low-cloud fraction  $LCF_i$   
 171 of weather state  $i$  as the total cloud fraction below 600 hPa. The monthly low-cloud frac-

172 tion is taken as

$$LCF = \sum_i f_i LCF_i, \quad (1)$$

173 where  $f_i$  is the frequency of weather state  $i$  over the month in question.

174 As described further below, all observational datasets are regredded conservatively  
 175 to a common  $2.8^\circ \times 2.8^\circ$  grid for analysis. We use observations covering the time pe-  
 176 riod between 1998-2023 for all datasets, except for cloud fraction (based on ISCCP), which  
 177 is limited to 1998-2017.

### 178 2.3 Quantifying Large-Scale Clustering of Heavy Precipitation

179 We quantify clustering of precipitation following Bläckberg & Singh (2022) using  
 180 daily surface precipitation in the tropics ( $30^\circ\text{S}$ - $30^\circ\text{N}$ ). To facilitate the comparison of clus-  
 181 tering across different models and the observations, we first interpolate the daily precipi-  
 182 tation to a  $2.8^\circ \times 2.8^\circ$  grid using a first-order conservative method (Jones, 1999) to pre-  
 183 serve tropical-mean properties from the native grid. Next we define heavily precipitat-  
 184 ing regions as gridboxes for which the precipitation rate exceeds a threshold. The thresh-  
 185 old is calculated as the 95th spatial percentile of daily precipitation over all gridboxes  
 186 in the tropics temporally averaged over the 30-year climatology (or 25-year in the case  
 187 of observations). For the GPCP observations, this threshold is  $16 \text{ mm day}^{-1}$ . Distinct  
 188 heavy precipitation features are identified as 8-connected contiguous regions of precipi-  
 189 tation exceeding the threshold or single grid boxes if there are no neighboring connec-  
 190 tions.

191 We define our primary measure of clustering,  $A_m$ , as the mean area of heavy pre-  
 192 cipitation features over the entire tropics.  $A_m$  conceptually captures clustering by dis-  
 193 tinguishing scenes with many small precipitation features and scenes where precipita-  
 194 tion is aggregated into fewer and/or larger precipitating features (Figure 1). The mean  
 195 area of features,  $A_m$ , was chosen due to its interpretability, however, we note that it is  
 196 only one aspect of the large-scale organization of precipitation, and  $A_m$  does not describe  
 197 important spatial characteristics such as the total area, shape, proximity, gradients of  
 198 precipitation intensity, and location of precipitation features. A number of other mea-  
 199 sures of large-scale clustering are analyzed and their interrelationship is presented in Fig-  
 200 ures S1-4 in the supporting information.

201 An important aspect of our method is that, by definition, regions of heavy precip-  
 202 itation occupy 5% of the domain on average. Thus when comparing two climates, the  
 203 mean area fraction of heavy precipitation  $\bar{A}_f$  remains constant. Differences in the mean  
 204 area of features,  $A_m$ , between climates are entirely due to a reorganization of precipi-  
 205 tation, and changes in  $A_m$  are inversely related to the mean number of precipitation fea-  
 206 tures. However, the above constraint does not apply to the precipitation distribution dur-  
 207 ing a given month. Indeed, as we shall see, an important driver of variations in tropi-  
 208 cal precipitation clustering in interannual variability is the area fraction of precipitation,  
 209  $A_f$ . We therefore consider the behavior of both the mean area of heavy precipitation fea-  
 210 tures,  $A_m$ , and the area fraction of heavy precipitation,  $A_f$ , in our analysis below.

### 211 2.4 Describing Relationships to Large-Scale Clustering of Heavy Pre- 212 cipitation

213 Having quantified large-scale precipitation clustering, we seek to characterize the  
 214 relationships between such clustering and other large-scale climate variables. Specifically,  
 215 we consider these relationships for interannual variability in both models and observa-  
 216 tions, and for changes in climate across the CMIP6 ensemble. Throughout, we define in-  
 217 terannual variability in a given variable by deseasonalized monthly anomalies, calculated  
 218 as the monthly-mean anomaly from the climatology of the associated month after de-

trending the time series. The trend is estimated by a first-order linear least squares regression of the data at each location from the daily (precipitation-based metrics) or monthly (all other metrics) time series.

As we will see, for interannual variability, the mean area of features,  $A_m$ , and the area fraction of precipitation,  $A_f$ , are strongly correlated with each other and to the large-scale climatic state. To estimate the individual effect of  $A_m$ , we apply the method of Pearson partial correlation (Mardia et al., 1979). The partial correlation  $r(X, Y|Z)$  represents the relationship between variables  $X$  and  $Y$  after the removal of the effect of  $Z$ , and is given by

$$r(X, Y|Z) = \frac{r(X, Y) - r(X, Z)r(Y, Z)}{\sqrt{1 - r^2(X, Z)}\sqrt{1 - r^2(Y, Z)}}, \quad (2)$$

where  $r(X, Y)$  is the regular correlation between  $X$  and  $Y$ . The significance of partial correlations is evaluated using the standard t-test for partial correlations.

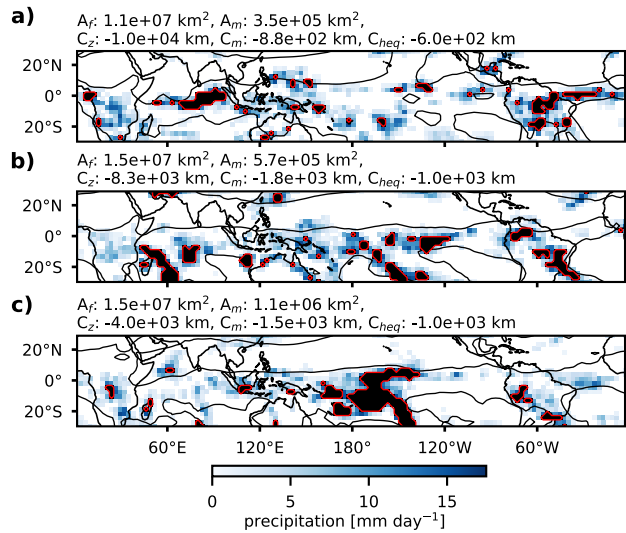


**Figure 1.** February daily snapshots of GPCP precipitation (blue colors) and regions of heavy precipitation (black shading) with monthly contour of ERA5 500 hPa relative humidity representing the median over the tropics (black line) and monthly ISCCP low cloud fraction (red colors). The panel titles show the total area of heavy precipitation as a fraction of the tropical domain area ( $A_f$ ), the mean area ( $A_m$ ) and number ( $N$ ) of heavy precipitation features, and the Oceanic Niño Index (ONI) taken from NOAA-GlobalTemp. From (a-c), clustering increases according to  $A_m$ . The clustering from (a-b) is primarily due to an increase in  $A_f$ , whereas the clustering from (b-c) is primarily due to the closer proximity of heavy precipitation to the central Pacific.

### 230    3 Spatial Patterns of Heavy Rainfall Clustering

231    The purpose of this section is to elucidate the spatial patterns of precipitation that  
 232    produce a high degree of clustering. We first consider how clustering changes in inter-  
 233    annual variability before we investigate the spatial patterns associated with strong in-  
 234    creases in clustering with warming across the CMIP6 ensemble.

235    Figure 2 shows the regression of monthly anomalies in the frequency of occurrence  
 236    of heavy precipitation,  $C$ , onto the mean area of heavy precipitation features,  $A_m$ , for  
 237    the observations. When tropical precipitation is observed to be highly clustered on the  
 238    large scale, heavy precipitation tends to occur more frequently in the central equatorial  
 239    Pacific. Figure 2 is calculated for all months, but similar spatial patterns can be seen  
 240    in individual months, strongest in DJF (Figure S5 in the supporting information). Other  
 241    notable spatial characteristics of the regression include a decrease in heavy precipitation  
 242    over the maritime continent and a small but statistically significant (crosses) decrease  
 243    in heavy precipitation over the Amazon and Atlantic.

244    To quantify the shift of heavy precipitation to the central equatorial Pacific, we de-  
 245    fine the distance metrics  $C_z$ , which represents the mean distance of heavily precipitat-  
 246    ing points within the tropics to the meridian given by the longitude  $180^\circ\text{E}$ , and  $C_m$ , which  
 247    represents a similar metric defined based on distance to the equator. These are some-  
 248    what arbitrary zonal and meridional reference lines with which to describe the zonal and  
 249    meridional shifts, and the clustering redistribution of heavy precipitation may be bet-  
 250    ter characterized relative to the climatological distribution. For example, in most mod-  
 251    els, with warming heavy precipitation moves south relative to the northern hemisphere  
 252    climatological convergence zone or north relative the climatological SPCZ or both. How-  
 253    ever, for simplicity, we use  $C_z$  and  $C_m$  defined based on  $180^\circ\text{E}$  and the equator.

254    As expected from the regression map, there is a strong relationship between the  
 255    mean area of features,  $A_m$ , and  $C_z$  (Figure S2 in the supporting information). However,  
 256    as shown in Figure 3a, there is also a strong observed relationship in interannual vari-  
 257    ability between  $A_m$  and the total area fraction of heavy precipitation,  $A_f$  [ $r^2(A_f, A_m) \sim$   
 258    0.7], with greater  $A_f$  favoring greater  $A_m$ . This suggests a large part of the observed re-  
 259    gression pattern is due to the effect of changes in the total precipitating area, rather than  
 260    a pure spatial redistribution of a fixed number of heavily precipitating points. This com-  
 261    plicates the interpretation of increased clustering in internal variability, since when com-  
 262    paring climates, the mean area fraction of heavy precipitation  $\bar{A}_f$  remains fixed at 0.05.  
 263    To address this, we estimate the variations in the distribution of heavy precipitation that  
 264    contribute to variations in  $A_m$  independent of changes in  $A_f$  using Pearson partial corre-  
 265    lation (see Methods).

266    Both  $C_z$  and  $C_m$  are negatively correlated with the mean area of heavy precipi-  
 267    tation features,  $A_m$ , when the effect of changes in the area fraction of heavy precipita-  
 268    tion,  $A_f$ , is removed (star in Figure 3b), suggesting that there is a shift of convection  
 269    toward the equator and the central Pacific when the tropics are highly clustered. For a  
 270    given  $A_f$ , this contraction of heavily precipitating regions explains about 5-10 percent  
 271    of the remaining variance after the effect of changes in  $A_f$  is removed.

272    Both the CMIP ensemble and the high-resolution model generally show similar spa-  
 273    tial patterns associated with increasing large-scale clustering (Figure 3b and Figure S6a-  
 274    b in the supporting information). All models show significant relationships between  $A_m$   
 275    and  $A_f$ , although generally somewhat weaker than in observations, and most models show  
 276    significant negative partial correlations between the distance metrics  $C_z$  (24/27 CMIP6  
 277    models) and  $C_m$  (22/27 CMIP6 models) after removing the effect of changes in  $A_f$  (Fig-  
 278    ure 3b). That is, as for the observations, most models agree that higher clustering, as  
 279    measured by a larger mean area of heavy precipitation features, is associated with a shift  
 280    in convection toward the central equatorial Pacific. Interestingly, the high-resolution GCM

<sup>281</sup> did not show a significant partial correlation with  $C_m$ , suggesting clustering in that model  
<sup>282</sup> is not sensitive to the meridional contraction of heavy precipitation to the equator.

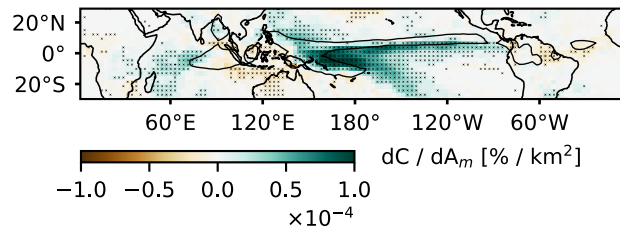


**Figure 2.** GPCP frequency of occurrence of heavy precipitation,  $C$ , regressed onto the mean area of heavy precipitation features,  $A_m$ , for interannual variability. The contour shows the 90th percentile of the climatological  $C$  and crosses indicate whether correlations are statistically significant.

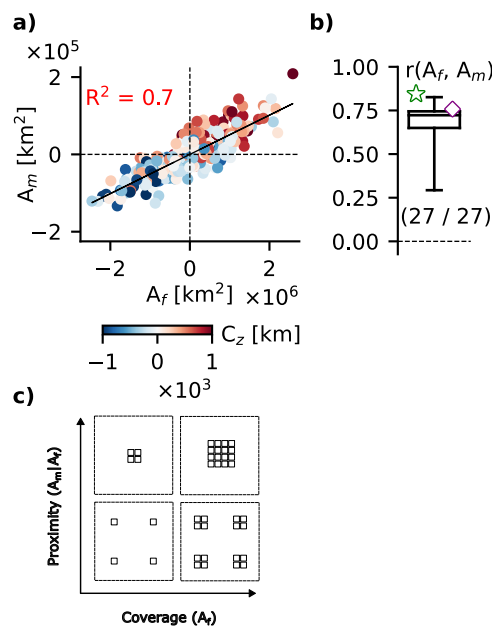


**Figure 3.** Scatter plot of monthly anomalies in area fraction of heavy precipitation,  $A_f$ , and the mean area of heavy precipitation features,  $A_m$ , colored by the zonal proximity of heavy precipitation to the longitude  $180^\circ$  E in the central pacific,  $C_z$ , for GPCP observations (a). Boxplot of the correlations between  $A_f$  and  $A_m$  and partial correlations of  $C_z$  and the proximity of heavy precipitation to the equator,  $C_m$ , with  $A_m$  outside the influence of  $A_f$  for the CMIP6 ensemble (b). The fraction of CMIP models with statistically significant correlations is indicated below each box, and the GPCP (star) and high-resolution GCM (diamond) correlations are shown in lighter colors if not statistically significant.

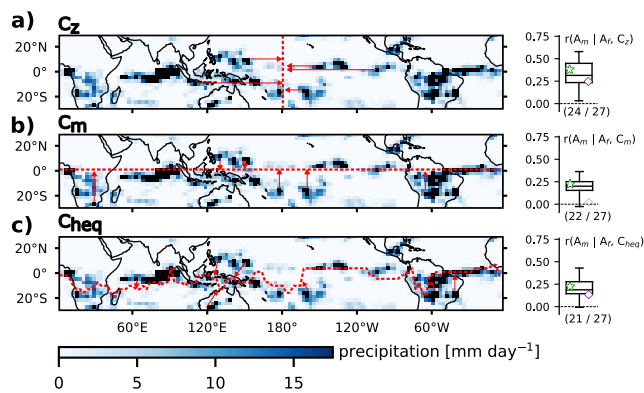


**Figure 4.** Scatter plot of monthly anomalies in area fraction of heavy precipitation,  $A_f$ , and the mean area of heavy precipitation features,  $A_m$ , colored by the zonal proximity of heavy precipitation to the longitude  $180^\circ$  E in the central pacific,  $C_z$ , for GPCP observations (a). Boxplot of the correlations between  $A_f$  and  $A_m$  and partial correlations of  $C_z$  and the proximity of heavy precipitation to the equator,  $C_m$ , with  $A_m$  outside the influence of  $A_f$  for the CMIP6 ensemble (b). The fraction of CMIP models with statistically significant correlations is indicated below each box, and the GPCP (star) and high-resolution GCM (diamond) correlations are shown in lighter colors if not statistically significant.

We now consider how large-scale clustering of heavy precipitation changes under climate change. Bläckberg & Singh (2022) noted that large-scale clustering increases as the climate warms in projections of climate change by the CMIP5 ensemble. Figure 5a shows that this is also true for CMIP6; all models project an increase in  $A_m$  with warming to varying degrees. However, there is a wide spread in climatological  $A_m$  and wide spread in climatological increase in  $A_m$  across the ensemble, suggesting the degree of large-scale clustering and the change in large-scale clustering with warming is poorly constrained in the models.

Given the climatologically fixed  $A_f$  in this framework, changes in the mean area of precipitation features,  $A_m$ , with warming are driven entirely by a spatial reorganization of convection to larger features. The present analysis evaluates whether the spatial patterns associated with a high degree of clustering of precipitation in interannual variability may also be relevant to the redistribution of heavy precipitation causing increased clustering under warming. Indeed, all but one model show a reduction in  $C_m$  with warming, indicating a contraction of heavy precipitation towards the equator (Figure 5b). Further, all models contract heavy precipitation towards the hydrological equator, or "ITCZ center", which is defined here as the latitude of highest specific humidity at 700 hPa as a function of longitude and time in months (Figure 5c). One possible interpretation of this is that a narrowing of the ITCZ provides a mechanism for the overall increase in clustering with warming. However, we note that the change in  $C_m$  with warming is uncorrelated with the change in  $A_m$  across the CMIP6 ensemble; models exhibiting stronger ITCZ narrowing with warming do not show stronger increases in large-scale clustering of precipitation. On the other hand, there is a significant correlation between increases in mean area of precipitation features,  $A_m$ , and changes in  $C_z$  across the CMIP6 ensemble. That is, models that show a greater clustering with warming also show a more zonal shift of heavy precipitation to the central Pacific (note that the zonal and meridional contractions are somewhat anticorrelated, as also identified by Popp & Bony (2019)).

Going beyond the simple distance metrics, Figure 6 regresses the projected increase in frequency of occurrence of heavy precipitation onto the projected increase in  $A_m$  across the CMIP ensemble. This reveals a spatial pattern of precipitation changes with several similarities to the pattern for interannual variability shown in Figure 2. However, an important distinction is that, for changes with warming, the redistribution of heavy precipitation is a conserved property, due to the climatologically fixed  $A_f$ . Similarities between the regression patterns include a regression coefficient largest in the central Pacific close to the equator, and a redistribution of precipitation away from the maritime continent, Amazon, and Atlantic. While under interannual variability heavy precipitation shifts southward in the Pacific for highly clustered states, the changes with warming show a northward shift of heavy precipitation in the Pacific.

We note that the spatial patterns associated with a climatologically high degree of clustering of heavy precipitation across the CMIP6 ensemble are rather different from those of internal variability and changes with warming (Figure S6c in the supporting information). Models with high climatological values of  $A_m$  tend to have more convection in the warm pool, over tropical continents, and at the edges of the northern and southern convergence zones over the Pacific Ocean. These relationships cannot be summarized by a single value of either  $C_z$  or  $C_m$ . Rather, we find that high climatological values of  $A_m$  are associated with high month-to-month variability in  $A_f$ . This indicates that high spatial clustering also corresponds to high clustering in time, with some days producing a large amount of heavy precipitation across the tropics and other days producing much less.

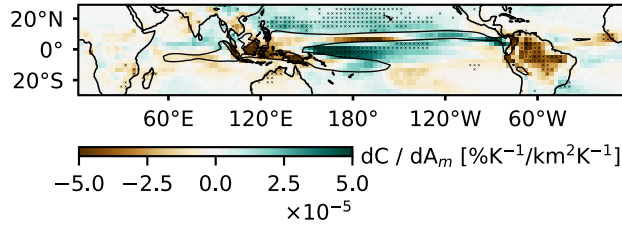


**Figure 5.** Scatter plot of change in climatological mean area of heavy precipitation features,  $A_m$ , with change in climatological mean distance of heavy precipitation to the central pacific,  $C_z$ , (a) and change in mean heavy precipitation proximity to the equator,  $C_m$  (b). Boxplot of change in climatological mean distance to the hydrological equator,  $C_{heq}$ , (c) where the hydrological equator is defined as the latitude of highest specific humidity at 700 hPa as a function of longitude and time in months. All quantities are normalized by the tropical surface temperature warming from the historical to the SSP585 scenario simulation period in CMIP6 models.

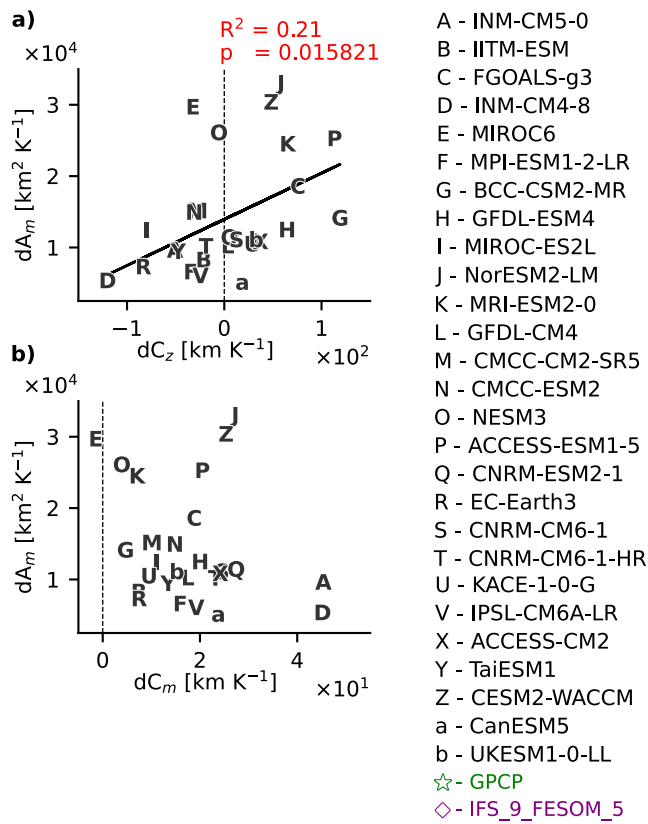


**Figure 6.** Increase in frequency of occurrence of heavy precipitation,  $C$ , regressed onto increase in  $A_m$  per kelvin tropical warming from the historical to the SSP585 scenario simulation period across the CMIP6 ensemble. Contour shows the ensemble-mean 90th percentile of  $C$  in the historical period and crosses indicate whether correlations are statistically significant.

332 In summary, the spatial patterns of heavy precipitation associated with highly clus-  
333 tered states vary across timescales, but there are important common threads. In both  
334 internal variability and for changes with warming, higher clustering as measured by  $A_m$   
335 is associated with more heavy precipitation in the central equatorial Pacific. In partic-  
336 ular, models with stronger increases in large-scale clustering of precipitation under warm-  
337 ing also exhibit greater zonal shifts in convection to the central Pacific. This potentially  
338 suggests the Walker circulation, and the East-West SST gradient in the Pacific, as an  
339 important control on the magnitude of changes in large-scale clustering of precipitation  
340 with warming. We next investigate the relationships between SST changes and changes  
341 in  $A_m$  in both internal variability and under climate change.

## 342 4 SST Drivers of Heavy Rainfall Clustering

343 This section investigates the extent to which changes in the El Niño-Southern Oscillation  
344 can explain changes in clustering across timescales. We use the Oceanic Niño Index (ONI; Sobel et al., 2002) to identify the state of the El Niño-Southern Oscillation  
345 in interannual variability. The ONI represents the three-month rolling average SST anomaly  
346 in the Niño3.4 region ( $5^{\circ}\text{S}$ -  $5^{\circ}\text{N}$ ,  $120^{\circ}$ - $170^{\circ}\text{W}$ ), calculated here relative to the full range  
347 of years used in the climatology. ONI values greater than  $0.5^{\circ}\text{C}$  represent El Niño conditions and ONI values less than  $-0.5^{\circ}\text{C}$  represent La Niña conditions. The climatological  
348 East-West Pacific SST gradient, defined as the time-mean difference between the SST  
349 in the western- ( $5^{\circ}\text{S}$  -  $5^{\circ}\text{N}$ ,  $80^{\circ}$  -  $150^{\circ}\text{E}$ ) and eastern ( $5^{\circ}\text{S}$  -  $5^{\circ}\text{N}$ ,  $180^{\circ}$  -  $80^{\circ}\text{W}$ ) Pacific boxes,  
350 which we denote  $T_z$ , serves as an indicator for climatologically “El Niño-like” conditions  
351 (Watanabe et al., 2024). Observations show several indications that highly clustered states,  
352 corresponding to large values of the mean area of heavy precipitation features,  $A_m$ , are  
353 associated with El Niño-like conditions. Firstly, SST regressed onto  $A_m$  for interannual  
354 variability shows a pattern strongly reminiscent of an El Niño SST signature (Alexander et al., 2002)  
355 (Figure 7). Secondly, during times of ONI exceeding  $0.5^{\circ}\text{C}$  compared to all days,  $A_m$  increases as heavy precipitation moves from the maritime continent towards the central Pacific (Figure S7b in supporting information). Finally, independent  
356 of changes in  $A_f$ , ONI shows a positive partial correlation with  $A_m$  (Figure 8a). Most  
357 CMIP models capture the observed connection between ONI and  $A_m$  (Figure S1 in the  
358 supporting information) and the independent contribution of ONI on  $A_m$  outside the influence  
359 of  $A_f$ , as does the high-resolution GCM (Figure S3 in the supporting information and Figure 8b). Thus both models and observations show that large-scale clustering  
360 of precipitation is stronger during El Niño than La Niña. This is despite the fact that  
361 El Niño represents a weakening of the Walker circulation and a weakening of tropical SST  
362 gradients, both of which are generally thought to facilitate the organization of convection  
363 on large scales.

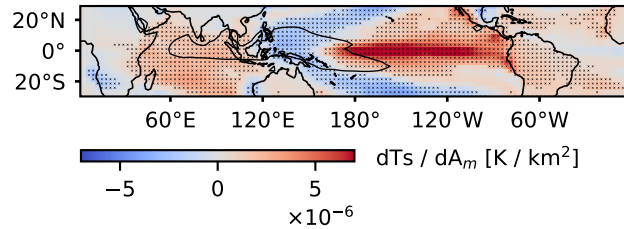


**Figure 7.** NOAA-GlobalTemp surface temperature,  $T_s$ , regressed onto  $A_m$  for interannual variability. The contour shows the climatological 90th percentile of  $T_s$ , and crosses indicate whether correlations are statistically significant.

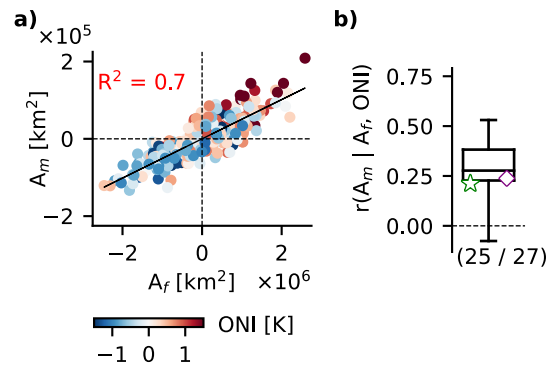


**Figure 8.** Same as Figure 3, but with the Oceanic Niño Index (ONI) in scatter colors and as explanatory variable in boxplot.

The strong connection between El Niño conditions and  $A_m$  in interannual variability motivates the investigation of changes in the climatological Pacific SST gradient to a more El Niño-like state as a mechanism for explaining model-spread in projected changes to clustering. Consistent with expectations, the magnitude of the weakening of the East-West Pacific SST gradient explains a similar amount of variance in projected changes in clustering as the zonal shift in heavy precipitation (Figure 9). Models that have more El Niño-like warming patterns tend to exhibit larger increases in large-scale clustering of precipitation. Regressing the SST changes against projected changes in the mean area of precipitation features,  $A_m$ , also shows an El-Niño-like pattern, with a relative warming in the east and relative cooling in the west (Figure 10). In addition, the regression pattern has a noticeable north-south gradient, consistent with the positive regression coefficients for heavy precipitation frequency north of the equator in Figure 6.

We have shown that El Niño-like states tend to result in a higher degree of clustering in both interannual variability and across the CMIP6 ensemble under climate change. Note, however, that there are changes in the zonal SST gradient,  $T_z$ , and the mean distance of heavy precipitation to the central Pacific of both signs across the 27 CMIP6 models we analyse, suggesting that zonal shifts in convection are not the primary reason for the ensemble-mean increase in large-scale clustering with warming that we document. We hypothesize that the ensemble-mean increase in  $A_m$  is instead associated with a meridional shift in convection, potentially related to a narrowing of the ITCZ (Byrne & Schneider, 2016). All but one model exhibit negative changes in  $C_m$  with warming, and this is associated with an increase in the large-scale clustering of precipitation in natural variability.

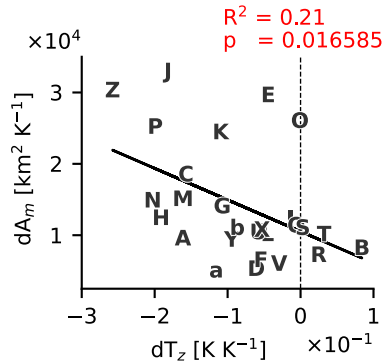


**Figure 9.** Same as Figure 4a, but with the change in the climatological Pacific SST gradient,  $T_z$ , per Kelvin tropical warming from the historical to the SSP585 scenario simulation period across the CMIP6 ensemble as explanatory variable. Models are as given in the legend in Figure 4.

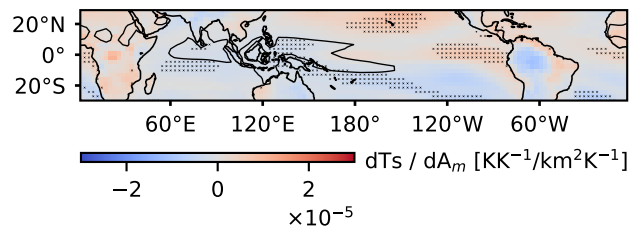


**Figure 10.** Change in surface temperature,  $T_s$ , regressed onto change in mean area of heavy precipitation features,  $A_m$ , per Kelvin tropical warming from the historical to the SSP585 scenario simulation period across the CMIP6 ensemble. Contour shows ensemble-mean 90th percentile climatological  $T_s$  and crosses indicate if correlations are statistically significant.

## 5 The Effect of Heavy Rainfall Clustering on Clouds and Humidity

We now consider how large-scale clustering of precipitation influences the cloud and humidity distribution. Our motivation is to understand how such clustering may influence radiative feedbacks. Previous authors have found that the degree of clustering on different spatial scales has an effect on the radiation budget and clouds (e.g., Bony et al., 2020; Wing & Emanuel, 2014; Pendergrass et al., 2016). The literature suggests changes in clustering under warming may lead to different cloud feedbacks and may therefore affect equilibrium climate sensitivity (ECS) (Schiro et al., 2022). This section investigates this hypothesis for large-scale clustering across the CMIP6 ensemble. As for previous sections, the analysis assesses whether relationships in interannual variability can be used to infer the response to climate change, raising the possibility of an observational constraint on particular radiative feedbacks or ECS itself.

Rather than focusing on changes in radiative fluxes or calculating feedback strength directly, we focus on changes in mid-tropospheric relative humidity, which has been argued to cause a negative longwave feedback associated with changes in convective organization (Tobin et al., 2013; Bony et al., 2020), and changes in low-cloud fraction in regions of subsidence, which have been argued to cause a positive shortwave feedback associated with changes in convective organization (Schiro et al., 2022). Changes in low clouds in regions of subsidence are also known to be important for understanding model spread in ECS (Zelinka et al., 2020). Correlations between measures of large-scale clustering of heavy precipitation and various other metrics commonly used to assess changes to the radiation budget on interannual and climatological timescales are presented in Figure S1-4 in the supporting information.

For our analysis, the mid-tropospheric relative humidity, RH, is taken as the 500 hPa value, but the conclusions are not sensitive to using proximate pressure levels down to 700 hPa. Observed low-cloud fraction, LCF, is calculated using the ISCCP weather states (Tselioudis et al., 2010) as described in Section 2.2, and taken as the cloud fraction below 600 hPa. CMIP6 low-cloud fraction is calculated analogously, with cloud fraction pre-processed by interpolating hybrid-sigma coordinates to 19 pressure levels if not already available on pressure levels. We also consider the mean low-cloud fraction in regions of descent, denoted by a subscript  $d$  and calculated as the mean of gridpoints for which the monthly-mean vertical pressure velocity at 500 hPa is positive. Later we will consider variables in regions of ascent, defined analogously for negative 500 hPa vertical velocity and identified by a subscript  $a$ .

Figure 11a and Figure 12a show observational estimates of the regression patterns of RH and LCF against the mean area of precipitation features,  $A_m$ , for interannual variability. The regressions show a clear El-Niño-like pattern, with increases in RH and decreases in LCF in the central and eastern Pacific, and opposite changes over the warm pool. This suggests the changes in RH and low clouds with increased tropical clustering are caused at least in part by variations associated with El Niño-Southern Oscillation.

From a tropics-wide perspective, when the observed degree of clustering is high according to  $A_m$ , the tropical mean is drier (Figure 11b) while LCF increases, both when averaged over descending grid points ( $LCF_d$  in Figure 12b) and in regions of time-mean descent (contour on Figure 12a). The environmental signature associated with large-scale clustering is therefore consistent with a negative longwave feedback identified for large-scale clustering in idealized simulations (Arnold & Randall, 2015) and a longwave- and low-cloud cooling signature found associated with interannual variations in mesoscale organization (Bony et al., 2020).

However, partial correlations of  $A_m$  with RH excluding the influence of the total area fraction of heavy precipitation,  $A_f$ , are insignificant in the observations (Figure 11b).

443 This suggests that the influence of  $A_m$  on relative humidity is almost entirely due to in-  
 444 creasing  $A_f$ . Observed correlations of relative humidity and the distance metrics  $C_m$  and  
 445  $C_z$ , representing proximity of heavy rainfall to the equator and the central Pacific, re-  
 446 spectively, are also generally insignificant. Observed  $LCF_d$  on the other hand increases  
 447 for all three forms of spatial clustering, outside the influence of  $A_f$  (Figure 12b).

448 The CMIP6 ensemble generally agrees on the strong association between  $A_f$  and  
 449 the aforementioned tropical environmental signatures. However, unlike the observational  
 450 estimates, about half of the models also show a significant relationship between relative  
 451 humidity and spatial shifts of heavy precipitation (Figure 11b). In particular, in a sub-  
 452 set of models, zonal shifts in heavy precipitation to the central Pacific are (independent  
 453 of variations in  $A_f$ ) associated with a moistening in the tropics, while meridional shifts  
 454 to the equator result in domain-mean drying. These relationships are also present in the  
 455 high-resolution GCM. The models generally do not capture the observed  $LCF_d$  signa-  
 456 ture for clustering outside the influence of  $A_f$ , except for a subset of CMIP models pro-  
 457 ducing increases in  $LCF_d$  for meridional shifts in heavy precipitation (Figure 12b).

458 Other notable independent effects of the spatial preference of heavy precipitation  
 459 on environmental conditions include a reduction in high cloud fraction above 400 hPa  
 460 in regions of ascent,  $HCF_a$ , with meridional shifts in precipitation ( $r(C_m, HCF_a | A_f) \sim$   
 461 0.25 in observations, the high-resolution GCM, and the model-mean of CMIP model cor-  
 462 relations).

463 Our analysis of interannual variability has revealed strong relationships between  
 464 RH and low-cloud fraction and large-scale clustering of precipitation in observations. How-  
 465 ever, in observations, the RH relationships are primarily driven by changes in the area  
 466 fraction of convection  $A_f$ .  $A_f$  also influences low cloud fraction,  $LCF_d$ , but spatial shifts  
 467 in heavy precipitation retains a connection to  $LCF_d$  outside the influence of  $A_f$  in ob-  
 468 servations. We now consider relationships between RH and low-cloud fraction changes  
 469 and changes in the clustering of precipitation in climate projections.

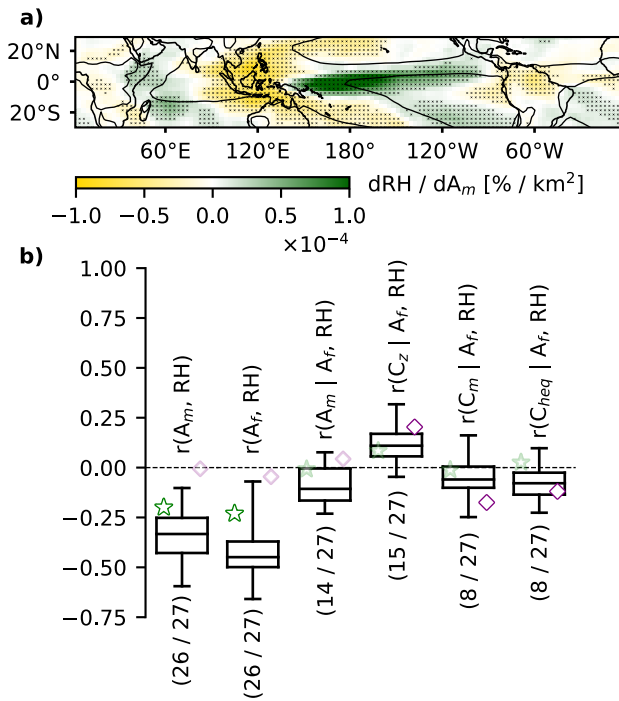


**Figure 11.** Relative humidity at 500 hPa, RH, regressed onto mean area of heavy precipitation features,  $A_m$ , in interannual variability (a). Boxplots of correlations and partial correlations outside the influence of the total area of heavy precipitation,  $A_f$ , of RH and  $A_m$ , mean distance of heavy precipitation to 180°E,  $C_z$ , and mean distance of heavy precipitation to the equator,  $C_m$  (b). Star and diamond show results for observations and high-resolution GCM, respectively, shown in lighter colors if not statistically significant. The numbers below the boxplots gives the fraction of models with statistically significant correlations.

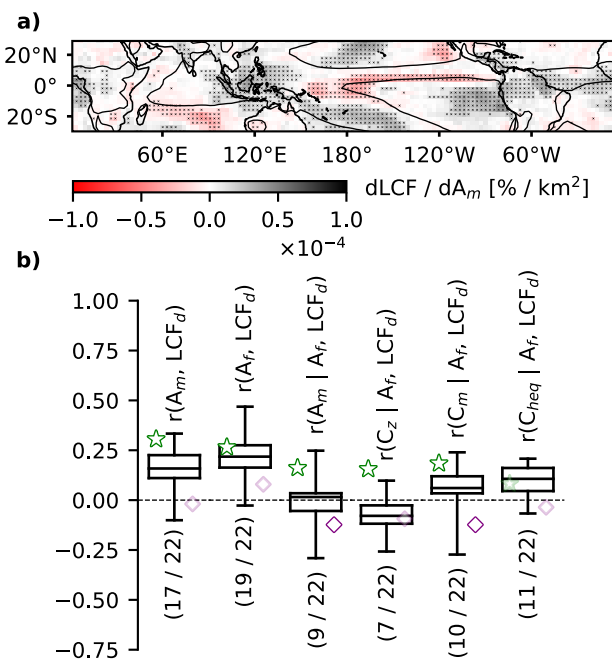


**Figure 12.** Same as Figure 10, but with the low cloud fraction, LCF, and low cloud fraction in regions of descent,  $\text{LCF}_d$ , as response variable.

470 Consistent with the results from the previous section, models with larger increases  
 471 in large-scale clustering under warming tend to have changes in relative humidity and  
 472 clouds consistent with an El Niño-like shift in the tropical circulation. The regression  
 473 patterns of RH and LCF onto changes in  $A_m$  under warming across the CMIP6 ensemble  
 474 (Figure S10a-b) are similar to those for interannual variability presented above. How-  
 475 ever, in contrast to the case for interannual variability, changes in large-scale clustering  
 476 with warming have little connection to changes in tropical-mean mean RH or low-cloud  
 477 fraction in regions of descent,  $LCF_d$ , across the CMIP6 ensemble (Figure 13a, b). Given  
 478 this, it is perhaps not surprising that there is no correlation between the increase in  $A_m$   
 479 within a model under warming and the model's ECS (Figure 13c). Here we take ECS  
 480 from the supplementary material of Zelinka et al. (2020) and Hausfather et al. (2022).

481 The results therefore indicate that changes in large-scale clustering under warm-  
 482 ing do not strongly affect radiative feedbacks, despite indications from observations that  
 483 more clustered states are drier with more low-clouds in regions of large-scale descent. One  
 484 reason for this result appears to be the different ways in which large-scale clustering can  
 485 manifest at different timescales. In interannual variability, increases in clustering are as-  
 486 sociated with increases in the fractional area of heavy precipitation, defined here by  $A_f$ .  
 487 Under climate change, increases in  $A_f$  in one month must be balanced by decreases in  
 488 another month such that the overall average must remain constant. When the effects of  
 489 changes in area fraction are removed, the observed relationship to RH becomes weak.  
 490 However, this explanation is not the whole story, as many of the models do exhibit changes  
 491 in RH associated with increased clustering independent of changes in the area fraction  
 492 of heavy precipitation. Even among this subset of models, however, future increases in  
 493  $A_m$  are not a good predictor of future changes in clouds or relative humidity. This sug-  
 494 gests that caution should be used in extrapolating relationships—either observed or simulated—  
 495 between large-scale clustering and other properties of the climate in internal variability  
 496 to those for climate change.

497 Finally, we note that there does exist a relationship between a tropical-mean dry-  
 498 ing and the proximity of heavy rainfall to the equator. Under warming, variations in the  
 499 meridional contraction of heavy rainfall, as measured by the mean distance of heavily  
 500 precipitating gridpoints to the equator  $C_m$ , explain about 45 percent of the variance in  
 501 tropical-mean drying (Figure 14c and Figure 15). This relationship is consistent with the  
 502 sign of the relationship between RH and  $C_m$  in interannual variability in a subset of CMIP6  
 503 models (Figure 11b). This result potentially highlights the importance of ITCZ narrow-  
 504 ing as a specific manifestation of large-scale clustering that appears to be important for  
 505 setting the tropical-mean relative humidity. However, we note that most of the spread  
 506 in projected drying is due to the result of four models with dramatically different dry-  
 507 ing trends, and thus further work is required to confirm if this relationship is robust and  
 508 physical.

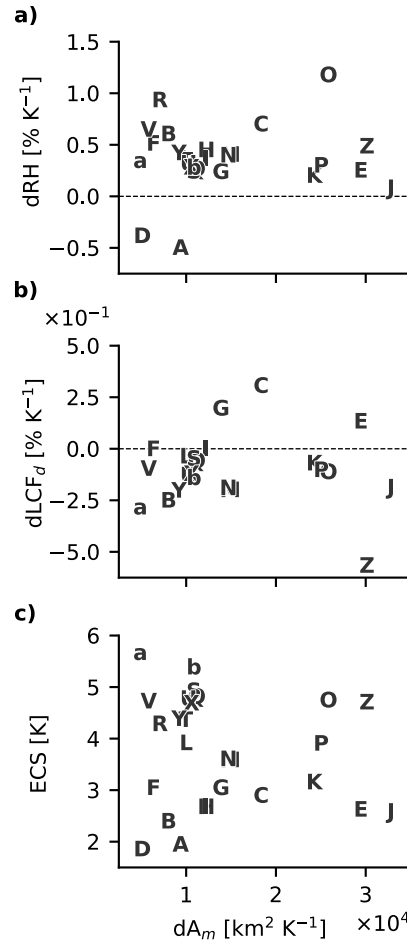


**Figure 13.** Scatter plot of change in  $A_m$  between historical period and SSP585 period per Kelvin tropical warming and associated tropical-mean change in 500 hPa relative humidity, RH, (a), low cloud fraction in regions of descent,  $LCF_d$  (b), and equilibrium climate sensitivity (ECS) in the CMIP6 ensemble (c). Models are as given in the legend in Figure 4.

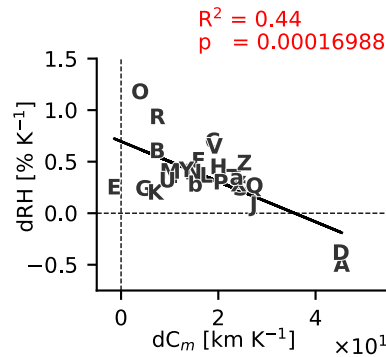


**Figure 14.** Change in relative humidity at 500 hPa, RH, regressed onto changes in mean distance of heavy precipitation to the equator,  $C_m$  between the historical and SSP585 periods per Kelvin warming.

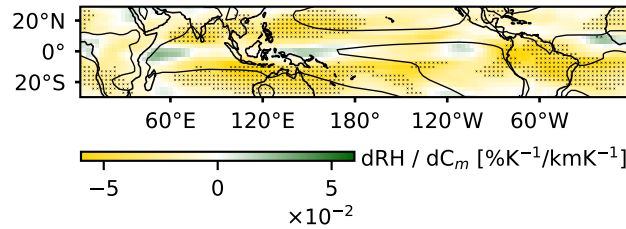


**Figure 15.** Scatter plot of change in mean distance of heavy precipitation to the equator,  $C_m$ , between historical period and SSP585 period per Kelvin tropical warming and associated tropical-mean change in 500hPa relative humidity, RH. The values are plotted as anomalies from the ensemble mean and models are as given in the legend in Figure 4.

509 **6 Summary and Discussion**

510 In this paper we have (1) presented the dominant spatial patterns of heavy pre-  
 511 cipitation that produce a high degree of clustering on the large scale (Section 3); (2) tied  
 512 the associated spatial patterns to mechanisms driving clustering through large-scale SST  
 513 patterns (Section 4); and (3) evaluated the associated changes in properties of the at-  
 514 mosphere that are important for the radiation budget (Section 5) in both interannual  
 515 variability and for projected changes with warming. We have defined the degree of clus-  
 516 tering of precipitation based on the spatial distribution of the top 5 percent heaviest daily  
 517 rainfall instances, with high clustering corresponding to scenes in which the mean area  
 518 of individual precipitation features is large. A challenge in any definition of convective  
 519 organization is in how one measures organization consistently as the total amount of pre-  
 520 cipitation changes (Retsch et al., 2020; Tobin et al., 2013). In the present study, the use  
 521 of a percentile precipitation threshold accounts for changing mean precipitation rates in  
 522 different climates. However, in internal variability, the area of precipitation features is  
 523 affected by both spatial shifts in the precipitation distribution and variations in the to-  
 524 tal area fraction of heavy precipitation,  $A_f$ . This is addressed here by using Pearson par-  
 525 tial correlations to evaluate the independent contributions of different measures of the  
 526 spatial distribution of precipitation while controlling for the effect of  $A_f$ .

527 When tropical precipitation is observed to be highly clustered on the large scale  
 528 in interannual variability, heavy precipitation gravitates meridionally to the equator and  
 529 zonally towards the central Pacific. In climate projections, large-scale clustering of pre-  
 530 cipitation is found to increase in all models, and this coincides with a shift of precipi-  
 531 tation toward the equator across the ensemble. We therefore hypothesize that a narrow-  
 532 ing of the ITCZ may be an important contributor to increases in large-scale clustering  
 533 of precipitation under warming. This implicates mechanisms related to the transport of  
 534 energy by the Hadley circulation that have been argued to control changes in ITCZ width  
 535 (Byrne & Schneider, 2016).

536 On the other hand, the intermodel spread in changes in clustering with warming  
 537 across the CMIP6 ensemble is related to zonal rather than meridional shifts in the pre-  
 538 cipitation. This motivated an investigation of the role played by Pacific SST gradients  
 539 in changes in large-scale clustering of precipitation. In interannual variability, El Niño-  
 540 Southern Oscillation linked variability appears to be a major driver of variability in large-  
 541 scale clustering of precipitation, with precipitation during El Niño events more clustered  
 542 than during La Niña events.

543 Under warming, changes in zonal SST gradients appeared to explain the sensitiv-  
 544 ity of projected clustering to zonal shifts in heavy rainfall; those models with more El  
 545 Niño-like warming patterns tended to exhibit stronger increases in precipitation cluster-  
 546 ing. This is important given the large disagreement between observed and simulated SST  
 547 trends in the topical Pacific (e.g., Wills et al., 2022). Observations show a strengthen-  
 548 ing of the SST gradient, suggesting a weaker increase in large-scale clustering compared  
 549 to simulations, which tend to show a weakening of tropical SST gradients.

550 Finally, we assessed if the changes in clustering with warming may have an influ-  
 551 ence on climate sensitivity. In observed interannual variability, a greater area fraction  
 552 of heavy precipitation,  $A_f$ , is associated with a drier domain-mean and an increase in  
 553 low-cloudiness in subsidence regions,  $LCF_d$ . The connection between clustering for a given  
 554  $A_f$  persists for  $LCF_d$ , but changes in the mean area of precipitation features and merid-  
 555 ional and zonal shifts in heavy precipitation generally have weak relationships to the tropical-  
 556 mean relative humidity, RH, independent of their relationship to  $A_f$ .

557 GCMs from the CMIP ensemble generally capture the observed tropical environ-  
 558 ment signatures associated with changes in  $A_f$ , but often have different RH and  $LCF_d$   
 559 connections to shifts in heavy precipitation independent of  $A_f$ . In contrast to observa-

tions, RH in several models is sensitive to both meridional and zonal shifts in heavy precipitation. In CMIP6 models, zonal shifts of precipitation to the central Pacific tend to moisten, whereas meridional shifts to the equator tend to dry. Realistically represented or not, these sensitivities appear to affect how these models project relative humidity into the future; the subset of models sensitive to drying from meridional contraction of heavy precipitation create considerable spread in the model ensemble relative humidity changes under warming.

The study includes several limitations that are worth highlighting. Perhaps most importantly, the models we examined do not resolve the processes leading to organization of convection on mesoscales, which in turn may affect how they simulate heavy precipitation associated with large-scale convective features (Bao et al., 2017). This includes the high-resolution GCM, which still employs a parameterized convection scheme (Koldunov et al., 2023). Another limitation is that monthly anomalies from the climatology of the associated month obscure variations in diurnal and daily clustering tendencies and seasonal differences in the strength of relationships. Similarly, the climatological values do not control for variations in the contribution from different timescales, including diurnal up to seasonal and decadal variations in clustering. Finally, we note that our model ensemble is one of opportunity, and the models used were dictated by the available data. Correlation across the ensemble is not guaranteed to be produced by a physical relationship, and the extent to which such relationships arise by chance rise the more variables are examined. Nevertheless, the relationships between SST gradients and shifts in the precipitation distribution we highlight here are based on well-established physical relationships that provides some confidence in their robustness.

Future research is encouraged to adopt the control for total convective area, or other similar controls for changes in the mean precipitation rate, as used in the present framework. One avenue for further investigation is to identify models with realistic clustering compared to observations. The CMIP6 models considered here show a wide range in climatological clustering and internal variability in clustering, and perhaps a subset of models with more realistic clustering characteristics should be given more weight in projections of climate. In a similar way, investigating the connection between large-scale clustering and mesoscale clustering in high-resolution observations and storm resolving models may further constrain the model spread in projections by identifying unrealistic behavior. Further developing these research endeavors would allow for increased confidence and reduce the model uncertainty in aspects of projections that could be influenced by changes in convective organization, ultimately allowing for improvement in mitigation and adaptation strategies for a warming climate.

**596 Open Research Section**

597 CMIP models used in this study are listed in Table S1 and model output is avail-  
598 able through the Earth System Grid Federation (ESGF) at <https://esgf-node.llnl.gov/search/cmip6/>.  
599 Observational datasets and access are listed here; GPCP precipitation dataset: <https://doi.org/10.5065/ZGJD-9B02>, ERA5 dataset: <https://doi.org/10.24381/cds.adbb2d47>, NOAA surface temper-  
600 ature dataset: <https://psl.noaa.gov/data/gridded/>, CERES outgoing longwave radia-  
601 tion dataset: <https://ceres.larc.nasa.gov/data/>, ISCCP: ISCCP cloud states dataset: <https://isccp.giss.nasa.gov/a>  
602 The IFS\_9\_FESOM\_5 model data is available via the World Data Center for Climate (WDCC)  
603 at DKRZ: [https://doi.org/10.26050/WDCC/nextGEMS\\_cyc2](https://doi.org/10.26050/WDCC/nextGEMS_cyc2). Code examples for repro-  
604 ducing key metric calculations and figures are available at Blackberg (2025a). Key met-  
605 rics are available at Blackberg (2025b).  
606

**Acknowledgments**

We acknowledge the World Climate Research Programme's Working Group on Coupled Modelling, which is responsible for CMIP, and we thank the climate modeling groups (listed in Table S1 in the supporting information) for producing and making available their model output. Further, we acknowledge the Deutsches Klimarechenzentrum (DKRZ) for providing resources for using the Levante supercomputer, which facilitated the analysis of the nextGEMS Cycle 2 simulation: IFS\_9\_FESOM\_5 used in this study. We also extend a special thank you to Dr. Cathy Hohenegger at Max Planck Institute for Meteorology for hosting the first author during a research visit to Hamburg, for providing guidance on model selection, and for facilitating access to institutional resources that greatly supported the analysis of the high-resolution GCM used in this study. Finally, we acknowledge support from the Australian Research Council (ARC) (grant no. DP230102077), the ARC Centre of Excellence for the Weather of the 21st Century (grant no. CE170100023), and computational resources and services from the National Computational Infrastructure, all funded by the Australian Government.

## 622 References

- Alexander, M. A., Bladé, I., Newman, M., Lanzante, J. R., Lau, N.-C., & Scott, J. D. (2002). The atmospheric bridge: The influence of enso teleconnections on air-sea interaction over the global oceans. *Journal of Climate*, 15(16), 2205 - 2231. Retrieved from [https://journals.ametsoc.org/view/journals/clim/15/16/1520-0442.2002.015.2205.tabtio\\_2.0.co\\_2.xml](https://journals.ametsoc.org/view/journals/clim/15/16/1520-0442.2002.015.2205.tabtio_2.0.co_2.xml) doi: 10.1175/1520-0442(2002)015<2205:TABTIO>2.0.CO;2
- Arnold, N. P., & Randall, D. A. (2015). Global-scale convective aggregation: Implications for the madden-julian oscillation. *Journal of Advances in Modeling Earth Systems*, 7(4), 1499-1518. Retrieved from <https://agupubs.onlinelibrary.wiley.com/doi/abs/10.1002/2015MS000498> doi: <https://doi.org/10.1002/2015MS000498>
- Bao, J., Sherwood, S. C., Colin, M., & Dixit, V. (2017, 10). The robust relationship between extreme precipitation and convective organization in idealized numerical modeling simulations. *Journal of Advances in Modeling Earth Systems*, 9, 2291-2303. Retrieved from <https://agupubs.onlinelibrary.wiley.com/doi/full/10.1002/2017MS001125> doi: 10.1002/2017MS001125
- Blackberg, P. (2025a). *Large-scale clustering of tropical precipitation: Code repository*. Zenodo. Retrieved from <https://doi.org/10.5281/zenodo.17070290> ([Software]) doi: 10.5281/zenodo.17070290
- Blackberg, P. (2025b). *Metrics for large-scale clustering of tropical precipitation*. Zenodo. Retrieved from <https://doi.org/10.5281/zenodo.16946243> ([Dataset]) doi: 10.5281/zenodo.16946243
- Bläckberg, C. P., & Singh, M. S. (2022, 5). Increased large-scale convective aggregation in cmip5 projections: Implications for tropical precipitation extremes. *Geophysical Research Letters*, 49. Retrieved from <https://agupubs.onlinelibrary.wiley.com/doi/full/10.1029/2021GL097295> doi: 10.1029/2021GL097295
- Bony, S., Semie, A., Kramer, R. J., Soden, B., Tompkins, A. M., & Emanuel, K. A. (2020). Observed modulation of the tropical radiation budget by deep convective organization and lower-tropospheric stability. *AGU Advances*, 1(3), e2019AV000155. Retrieved from <https://agupubs.onlinelibrary.wiley.com/doi/abs/10.1029/2019AV000155> (e2019AV000155 10.1029/2019AV000155) doi: <https://doi.org/10.1029/2019AV000155>
- Bretherton, C. S., Blossey, P. N., & Khairoutdinov, M. (2005, December). An energy-balance analysis of deep convective self-aggregation above uniform sst. *Journal of the Atmospheric Sciences*, 62(12), 4273-4292. Retrieved from <http://dx.doi.org/10.1175/JAS3614.1> doi: 10.1175/jas3614.1
- Byrne, M. P., & Schneider, T. (2016). Energetic constraints on the width of the intertropical convergence zone. *Journal of Climate*, 29(13), 4709 - 4721. Retrieved from <https://journals.ametsoc.org/view/journals/clim/29/13/jcli-d-15-0767.1.xml> doi: 10.1175/JCLI-D-15-0767.1
- Emanuel, K., Wing, A. A., & Vincent, E. M. (2014, 2). Radiative-convective instability. *Journal of Advances in Modeling Earth Systems*, 6(1), 75-90. Retrieved from <http://dx.doi.org/10.1002/2013ms000270> doi: 10.1002/2013ms000270
- Eyring, V., Bony, S., Meehl, G. A., Senior, C. A., Stevens, B., Stouffer, R. J., & Taylor, K. E. (2016). Overview of the coupled model intercomparison project phase 6 (cmip6) experimental design and organization. *Geoscientific Model Development*, 9(5), 1937-1958. Retrieved from <https://gmd.copernicus.org/articles/9/1937/2016/> doi: 10.5194/gmd-9-1937-2016
- Hartmann, D. L., Hendon, H. H., & Houze, R. A. (1984). Some implications of the mesoscale circulations in tropical cloud clusters for large-scale dynamics and climate. *Journal of Atmospheric Sciences*, 41, 113 - 121. Retrieved from [https://journals.ametsoc.org/view/journals/atsc/41/1/1520-0469\\_1984\\_041\\_0113\\_siotmc\\_2.0\\_co\\_2.xml](https://journals.ametsoc.org/view/journals/atsc/41/1/1520-0469_1984_041_0113_siotmc_2.0_co_2.xml) doi: 10.1175/1520-0469(1984)041<0113:

- 676 SIOTMC>2.0.CO;2
- 677 Hausfather, Z., Marvel, K., Schmidt, G. A., Nielsen-Gammon, J. W., & Zelinka, M.  
678 (2022). Climate simulations: Recognize the ‘hot model’ problem. *Nature*, *605*,  
679 26–29. doi: 10.1038/d41586-022-01192-2
- 680 Hersbach, H., Bell, B., Berrisford, P., Horányi, A., Muñoz-Sabater, J., Nicolas, J., ...  
681 Thépaut, J.-N. (2023). *Era5 hourly data on pressure levels from 1940 to present*.  
682 Copernicus Climate Change Service (C3S) Climate Data Store. Retrieved from  
683 <https://cds.climate.copernicus.eu/datasets/reanalysis-era5-pressure-levels> (Accessed: 2025-05-07) doi: 10.24381/cds.bd0915c6
- 684 Holloway, C. E., Wing, A. A., Bony, S., Muller, C., Masunaga, H., L'Ecuyer, T. S.,  
685 ... Zuidema, P. (2017, November). Observing convective aggregation. *Surveys  
686 in Geophysics*, *38*(6), 1199–1236. Retrieved from <https://link.springer.com/article/10.1007/s10712-017-9419-1> doi: 10.1007/s10712-017-9419-1
- 687 Huang, B., Yin, X., Menne, M. J., Vose, R. S., & Zhang, H.-M. (2024). *Noaa global  
688 surface temperature dataset (noaglobaltemp), version 6.0.* NOAA National Cen-  
689 ters for Environmental Information. Retrieved from <https://www.ncei.noaa.gov/access/metadata/landing-page/bin/iso?id=gov.noaa.ncdc%3AC01704>  
690 doi: 10.25921/rzxg-p717
- 691 Huffman, G. J., Adler, R. F., Behrangi, A., Bolvin, D. T., Nelkin, E. J., Gu, G.,  
692 & Ehsani, M. R. (2023). *The new version 3.2 global precipitation climatol-  
693 ogy project (gpcp) monthly and daily precipitation products* (Vol. 36) (No. 21).  
694 American Meteorological Society. Retrieved from <https://doi.org/10.1175/JCLI-D-23-0123.1> doi: 10.1175/JCLI-D-23-0123.1
- 695 Jones, P. W. (1999). First- and second-order conservative remapping schemes  
696 for grids in spherical coordinates. *Monthly Weather Review*, *127*(9), 2204  
697 - 2210. Retrieved from [https://journals.ametsoc.org/view/journals/mwre/127/9/1520-0493\\_1999\\_127\\_2204\\_fasocr\\_2.0.co\\_2.xml](https://journals.ametsoc.org/view/journals/mwre/127/9/1520-0493_1999_127_2204_fasocr_2.0.co_2.xml) doi: 10.1175/1520-0493(1999)127<2204:FASOCR>2.0.CO;2
- 698 Koldunov, N., Kölling, T., Pedruzo-Bagazgoitia, X., Rackow, T., Redler, R.,  
699 Sidorenko, D., ... Ziemen, F. A. (2023). *nextgems: output of the model de-  
700 velopment cycle 3 simulations for icon and ifs.* World Data Center for Cli-  
701 mate (WDCC) at DKRZ. Retrieved from [https://doi.org/10.26050/WDCC/nextGEMS\\_cyc3](https://doi.org/10.26050/WDCC/nextGEMS_cyc3) doi: 10.26050/WDCC/nextGEMS\_cyc3
- 702 Maddox, R. A. (1980, November). Mesoscale convective complexes. *Bulletin of  
703 the American Meteorological Society*, *61*(11), 1374–1387. Retrieved from [http://dx.doi.org/10.1175/1520-0477\(1980\)061<1374:MCC>2.0.CO;2](http://dx.doi.org/10.1175/1520-0477(1980)061<1374:MCC>2.0.CO;2) doi: 10.1175/1520-0477(1980)061<1374:mcc>2.0.co;2
- 704 Mapes, B. E. (1993, July). Gregarious tropical convection. *Journal of the At-  
705 mospheric Sciences*, *50*(13), 2026–2037. Retrieved from [http://dx.doi.org/10.1175/1520-0469\(1993\)050<2026:gtc>2.0.co;2](http://dx.doi.org/10.1175/1520-0469(1993)050<2026:GTC>2.0.CO;2) doi: 10.1175/1520-0469(1993)  
706 050<2026:gtc>2.0.co;2
- 707 Mapes, B. E., & Houze, R. A. (1993, May). Cloud clusters and superclusters  
708 over the oceanic warm pool. *Monthly Weather Review*, *121*(5), 1398–1416.  
709 Retrieved from [http://dx.doi.org/10.1175/1520-0493\(1993\)121<1398:ccasot>2.0.co;2](http://dx.doi.org/10.1175/1520-0493(1993)121<1398:CCASOT>2.0.CO;2) doi: 10.1175/1520-0493(1993)121<1398:ccasot>2.0.co;2
- 710 Mardia, K. V., Kent, J. T., & Bibby, J. M. (1979). *Multivariate analysis*. London:  
711 Academic Press.
- 712 NOAA Physical Sciences Laboratory, Climate Prediction Center. (2025). *Cpc  
713 daily blended outgoing longwave radiation (olr) – 1° × 1°.* <https://psl.noaa.gov/data/gridded/data.cpc.blended.olr-1deg.html>. (Daily OLR data  
714 (1991–present); please acknowledge NOAA PSL when using)
- 715 Pendergrass, A. G., Reed, K. A., & Medeiros, B. (2016). The link between extreme  
716 precipitation and convective organization in a warming climate: Global radiative-  
717 convective equilibrium simulations. *Geophysical Research Letters*, *43*(21), 11,445-

- 730        11,452. Retrieved from <https://agupubs.onlinelibrary.wiley.com/doi/abs/10.1002/2016GL071285> doi: <https://doi.org/10.1002/2016GL071285>
- 731        Popp, M., & Bony, S. (2019). Stronger zonal convective clustering associated with a  
732        wider tropical rain belt. *Nature Communications*, 10, 4261. doi: 10.1038/s41467-019-12167-9
- 733        Quan, H., Zhang, B., Wang, C., & Fueglistaler, S. (2025). The sea surface tem-  
734        perature pattern effect on outgoing longwave radiation: The role of large-scale  
735        convective aggregation. *Geophysical Research Letters*, 52(11), e2024GL112756.  
736        Retrieved from <https://agupubs.onlinelibrary.wiley.com/doi/abs/10.1029/2024GL112756> (e2024GL112756 2024GL112756) doi: <https://doi.org/10.1029/2024GL112756>
- 737        Retsch, M. H., Jakob, C., & Singh, M. S. (2020, 4). Assessing convective organiza-  
738        tion in tropical radar observations. *Journal of Geophysical Research: Atmospheres*,  
739        125. doi: 10.1029/2019JD031801
- 740        Schiro, K., Su, H., Ahmed, F., Dai, N., Singer, C., Gentine, P., ... Neelin, J.  
741        (2022, 11). Model spread in tropical low cloud feedback tied to overturning  
742        circulation response to warming. *Nature Communications*, 13, 7119. Retrieved  
743        from <https://www.nature.com/articles/s41467-022-34787-4> doi:  
744        10.1038/s41467-022-34787-4
- 745        Semie, A. G., & Bony, S. (2020). Relationship between precipitation extremes  
746        and convective organization inferred from satellite observations. *Geophysical  
747        Research Letters*, 47(9), e2019GL086927. Retrieved from <https://agupubs.onlinelibrary.wiley.com/doi/abs/10.1029/2019GL086927> (e2019GL086927  
748        10.1029/2019GL086927) doi: <https://doi.org/10.1029/2019GL086927>
- 749        Sobel, A. H., Held, I. M., & Bretherton, C. S. (2002). The enso signal in tropical  
750        tropospheric temperature. *Journal of Climate*, 15(18), 2702 - 2706. Retrieved  
751        from [https://journals.ametsoc.org/view/journals/clim/15/18/1520-0442\\_2002\\_015\\_2702\\_tesitt\\_2.0.co\\_2.xml](https://journals.ametsoc.org/view/journals/clim/15/18/1520-0442_2002_015_2702_tesitt_2.0.co_2.xml) doi: 10.1175/1520-0442(2002)015<2702:TESITT>2.0.CO;2
- 752        Tobin, I., Bony, S., Holloway, C. E., Grandpeix, J.-Y., Sèze, G., Coppin, D., ...  
753        Roca, R. (2013). Does convective aggregation need to be represented in cumulus  
754        parameterizations? *Journal of Advances in Modeling Earth Systems*, 5(4), 692-  
755        703. Retrieved from <https://agupubs.onlinelibrary.wiley.com/doi/abs/10.1002/jame.20047> doi: <https://doi.org/10.1002/jame.20047>
- 756        Tselioudis, G., Tromeur, E., Rossow, W. B., & Zerefos, C. S. (2010, 7). Decadal  
757        changes in tropical convection suggest effects on stratospheric water vapor. *Geo-  
758        physical Research Letters*, 37. doi: 10.1029/2010GL044092
- 759        Watanabe, M., Kang, S. M., Collins, M., Hwang, Y.-T., McGregor, S., & Stuecker,  
760        M. F. (2024). Possible shift in controls of the tropical pacific surface warming  
761        pattern. *Nature*, 630(8016), 315–324. Retrieved from <https://www.nature.com/articles/s41586-024-07452-7> doi: 10.1038/s41586-024-07452-7
- 762        Wheeler, M., & Kiladis, G. N. (1999). Convectively coupled equatorial waves: Anal-  
763        ysis of clouds and temperature in the wavenumber-frequency domain. *Journal  
764        of the Atmospheric Sciences*, 56, 374-399. Retrieved from [https://journals.ametsoc.org/view/journals/atsc/56/3/1520-0469\\_1999\\_056\\_0374\\_ccewao\\_2.0.co\\_2.xml](https://journals.ametsoc.org/view/journals/atsc/56/3/1520-0469_1999_056_0374_ccewao_2.0.co_2.xml) doi: 10.1175/1520-0469(1999)056<0374:CCEWAO>2.0.CO;2
- 765        Williams, A. I. L., Jeevanjee, N., & Bloch-Johnson, J. (2023). Circus tents, con-  
766        vective thresholds, and the non-linear climate response to tropical ssts. *Geophys-  
767        ical Research Letters*, 50(6), e2022GL101499. Retrieved from <https://agupubs.onlinelibrary.wiley.com/doi/abs/10.1029/2022GL101499> (e2022GL101499  
768        2022GL101499) doi: <https://doi.org/10.1029/2022GL101499>
- 769        Wills, R. C. J., Dong, Y., Proistosecu, C., Armour, K. C., & Battisti, D. S. (2022,  
770        September). Systematic climate model biases in the large-scale patterns of recent  
771        sea-surface temperature and sea-level pressure change. *Geophysical Research Let-*

- ters, 49(17). Retrieved from <http://dx.doi.org/10.1029/2022GL100011> doi: 10.1029/2022gl100011
- Wing, A. A., Emanuel, K., Holloway, C. E., & Muller, C. (2018). Convective self-aggregation in numerical simulations: A review. In R. Pincus, D. Winker, S. Bony, & B. Stevens (Eds.), *Shallow clouds, water vapor, circulation, and climate sensitivity* (pp. 1–25). Cham: Springer International Publishing. Retrieved from [https://doi.org/10.1007/978-3-319-77273-8\\_1](https://doi.org/10.1007/978-3-319-77273-8_1) doi: 10.1007/978-3-319-77273-8\_1
- Wing, A. A., & Emanuel, K. A. (2014). Physical mechanisms controlling self-aggregation of convection in idealized numerical modeling simulations. *Journal of Advances in Modeling Earth Systems*, 6(1), 59–74. Retrieved from <https://agupubs.onlinelibrary.wiley.com/doi/abs/10.1002/2013MS000269> doi: <https://doi.org/10.1002/2013MS000269>
- Wodzicki, K. R., & Rapp, A. D. (2016). Long-term characterization of the pacific itcz using trmm, gpcp, and era-interim. *Journal of Geophysical Research: Atmospheres*, 121(7), 3153–3170. Retrieved from <https://agupubs.onlinelibrary.wiley.com/doi/abs/10.1002/2015JD024458> doi: <https://doi.org/10.1002/2015JD024458>
- Young, A. H., Knapp, K. R., Inamdar, A., Hankins, W., & Rossow, W. B. (2018). The international satellite cloud climatology project h-series climate data record product. *Earth System Science Data*, 10(1), 583–593. Retrieved from <https://essd.copernicus.org/articles/10/583/2018/> doi: 10.5194/essd-10-583-2018
- Zelinka, M. D., Myers, T. A., McCoy, D. T., Po-Chedley, S., Caldwell, P. M., Ceppli, P., ... Taylor, K. E. (2020). Causes of higher climate sensitivity in cmip6 models. *Geophysical Research Letters*, 47(1), e2019GL085782. Retrieved from <https://agupubs.onlinelibrary.wiley.com/doi/full/10.1029/2019GL085782>